Journal of Advanced Ceramics
2024, **13**(4): 437–446
https://doi.org/10.26599/JAC.2024.9220866

Research Article

Macroscopic polarization enhancement boosting piezo-photocatalytic performance via Nb-doping on B-site of $Bi_4Ti_3O_{12}$ nanosheets

Hongjian Yu[1,✉], Xindong Wei[1], Min Wang[1], Yan Zhang[1,2], Zheng Wu[3,✉], Fan Guo[1], Jie Han[1,✉]

[1] *School of Chemistry and Chemical Engineering, Yangzhou University, Yangzhou 225002, China*
[2] *Engineering Research Center of Ministry of Education for Geological Carbon Storage and Low Carbon Utilization of Resources, Beijing Key Laboratory of Materials Utilization of Nonmetallic Minerals and Solid Wastes, National Laboratory of Mineral Materials, School of Material Sciences and Technology, China University of Geosciences (Beijing), Beijing 100083, China*
[3] *School of Environmental and Chemical Engineering, Xi'an Key Laboratory of Textile Chemical Engineering Auxiliaries, Xi'an Polytechnic University, Xi'an 710048, China*

Received: December 22, 2023; Revised: February 15, 2024; Accepted: February 15, 2024

Abstract: The development of a high-performance ferroelectric piezo-photocatalyst is an efficient strategy for advancing sustainability within the environmental and energy sectors. Yet, a major challenge lies in the creation of a strong polarized electric field that can effectively hinder charge recombination, both within the bulk and on the surface of catalysts. Herein, we synthesize a series of Nb-doped $Bi_4Ti_3O_{12}$ nanosheets via a facile one-pot hydrothermal method to achieve synergistically enhanced piezo-photocatalytic performance in CO_2 reduction and pollutant degradation. The optimized doped $Bi_4Ti_3O_{12}$ demonstrates remarkable efficiency in the conversion of CO_2 into CO, with a high production rate of 72.7 $\mu mol \cdot g^{-1} \cdot h^{-1}$ without using co-catalysts or any sacrificial agent, surpassing the performance of unmodified $Bi_4Ti_3O_{12}$ by up to 4.69 folds. Additionally, our catalyst demonstrates ultra-fast piezo-photocatalytic degradation of organic pollutant Rhodamine B (RhB) at low concentrations and exceptional piezo-photocatalytic activity at high concentrations, outperforming most previously reported state-of-the-art catalysts. The systematic corroboration of catalyst characterization and experimental analysis reveals that the synergistic effect arises from the amplified macroscopic polarization induced by lattice distortion caused by the larger Nb ions, thereby improving piezo-photocatalytic efficiency. This research thus offers valuable insights into the direct design and fabrication of versatile catalytic systems, with applications spanning CO_2 valorization and beyond.

Keywords: Nb-doped $Bi_4Ti_3O_{12}$; piezo-photocatalysis; CO_2 reduction; dye degradation; macroscopic polarization regulation

1 Introduction

The widespread use of fossil fuels has resulted in an energy crisis, worldwide environmental pollution, and global greenhouse effects, endangering the sustainable development of human civilization [1–4]. To tackle these challenges, semiconductor-based photocatalytic technologies have emerged as a promising avenue, offering the prospect of harnessing abundant solar energy for practical applications [5–8]. However, a significant challenge lies in achieving efficient separation of photo-generated electrons and holes, both in bulk and on the surface of photocatalysts [9–11]. In recent decades, substantial efforts have been made to enhance photocatalytic efficiency, focusing on strategies such as shape-controlled growth, creating heterojunctions, introducing defects, and elemental doping [12–15].

Piezoelectric materials, characterized by their unique crystal structures that can generate polarization charges in response to mechanical stress or deformation (tidal, environmental noise, wind energy, etc.), have opened up tremendous opportunities for converting mechanical energy to chemical energy [16–19]. Several piezoelectric semiconductor materials, such as ZnO [20], MoS_2 [21], C_3N_4 [22], and polyvinylidene fluoride (PVDF) [23], have exhibited excellent piezocatalytic performance across diverse applications ranging from the breakdown of organic pollutants to water splitting, CO_2 reduction, and pathogen inactivation [24–28]. More importantly, the internal electric field induced by the piezoelectric polarized charges creates an energetic driving force that facilitates efficient separation and controlled migration of the photo-generated carriers within the space charge region [29]. This synergy between piezoelectric polarization and photocatalysis thus offers the benefits of low energy consumption, ease of control, and low cost compared to traditional semiconductors [30]. Yet, it remains a challenge to enhance the internal polarization of piezoelectric semiconductors and control the energy band structure which can accelerate the separation and migration of photogenerated electrons and holes.

In recent years, ferroelectric and piezoelectric semiconductors have emerged as high-performance photocatalysts owing to their inherent polarized electric fields, resulting in the coupling of

✉ Corresponding authors.
E-mail: H. Yu, yhj@yzu.edu.cn;
Z. Wu, wuzheng@xpu.edu.cn;
J. Han, hanjie@yzu.edu.cn

mechanical and solar energy to achieve breakthrough catalytic conversion efficiency [31–34]. Traditional semiconducting ferroelectrics such as $BaTiO_3$ [35], $NaNbO_3$ [36], $SrTiO_3$ [37], and $BiFeO_3$ [38] have been explored as effective piezo- or photocatalysts. Amongst these, the bismuth layer-structured ferroelectrics (BLSFs) have gained prominence due to their unique electronic band structure and remarkable piezoelectric and ferroelectric properties which facilitate interlayer charge migration and transfer [39]. $Bi_4Ti_3O_{12}$ is a typical representative of BLSFs that has exceptional piezoelectric and ferroelectric properties and has exhibited excellent piezocatalytic and photocatalytic performance in CO_2 reduction, pollutant degradation, and molecular oxygen activation [40–42]. To further optimize the catalytic performance, various strategies have been employed [43–45]. Element doping is regarded as an effective and simple method to modulate the polarization of ferroelectric materials. Bai *et al.* [46] proposed a strategy to control the band structure and enhance the polarity via heterovalent ion doping of $BaTiO_3$. The optimized Li-doped $BaTiO_3$ and La-doped $BaTiO_3$ exhibited a significant enhancement for hydrogen evolution and achieved specific pollutant degradation because the acceptor (Li^+) or donor (La^{3+}) dopants endow different thermodynamic driving forces for the redox reactions [46]. In addition, Zhu *et al.* [47] prepared Fe-doped $Bi_4Ti_3O_{12}$ (Fe/BTO) nanosheets with exposed {001} facets by molten salt method. Compared with pure BTO, the 2%Fe/BTO sample exhibits the highest photocatalytic activity for photodegradation of phenol and bisphenol A under light irradiation. The depolarisation fields and photogenerated carriers trapped by Fe^{3+} co-inhibit recombination of electrons and holes, thus improving the photocatalytic performance [47]. Despite these promising outcomes, the development of a high-performance $Bi_4Ti_3O_{12}$ piezo-photocatalyst through appropriate ion doping remains unexplored, underscoring the need for an in-depth understanding of the relationship between polarization enhancement and piezo-photocatalysis [48,49].

Herein, we present a facile one-step hydrothermal method for the synthesis of a series of niobium (Nb)-doped $Bi_4Ti_3O_{12}$ (Nb-doped BTO) nanosheets. The deliberate addition of Nb ions, which have a larger ion radius and higher valence, induces lattice distortion in BTO, thereby enhancing the polarization field which drives the separation and migration of photo-generated carriers. Remarkably, our optimized 5% Nb-doped BTO demonstrates a substantial enhancement in CO_2 piezo-photoreduction activity, achieving a CO production rate of 72.7 $\mu mol \cdot g^{-1} \cdot h^{-1}$ without requiring co-catalysts or sacrificial agent, ~4.69 times improvement compared to unmodified BTO. Moreover, our optimized catalyst displays exceptional efficiency in the rapid degradation of an organic pollutant Rhodamine B (RhB) at concentrations of both 5 and 500 $mg \cdot L^{-1}$. Notably, we also elucidate the underlying mechanisms through comprehensive polarization analysis and electrochemical tests. Hence, our strategic approach has the potential to inspire further research into the development of highly efficient piezo-photocatalysts for applications such as energy conversion and environmental remediation.

2 Experimental

2.1 Chemicals

All chemicals used in this work are analytical grade without further purification. Bismuth nitrate pentahydrate ($Bi(NO_3)_3 \cdot 5H_2O$, AR), titanium oxide (TiO_2, AR), niobium pentoxide (Nb_2O_5, AR), sodium hydroxide (NaOH, AR), sodium sulfate (Na_2SO_4, AR), silver nitrate ($AgNO_3$, AR), L(+)-Ascorbic acid (LAA, AR), isopropyl alcohol (IPA, AR), and ethylene diamine tetraacetic acid disodium salt (EDTA-2Na, AR) were purchased from Sinopharm Chemical Reagent (China). Carbon dioxide (CO_2, ≥ 99.999%) was purchased from Nanjing Lian Yang Gas (China). Rhodamine B (RhB, AR), methyl orange (MO, AR), methylene blue (MB, AR), bisphenol A (BPA, AR), tetracycline hydrochloride (TC, AR), and 5,5-dimethyl-l-pyrroline N-oxide (DMPO, AR) were purchased from Macklin Biochemical (China). Deionized water was employed throughout the experiments.

2.2 Synthesis of $Bi_4Ti_3O_{12}$ nanosheets

4 mmol $Bi(NO_3)_3 \cdot 5H_2O$ (1.9400 g), 3 mmol TiO_2 (0.2396 g), and 0.12 mol NaOH (4.800 g) were added into 30 mL of deionized water and stirred for 30 min at room temperature. Then, the above slurry was transferred to a Teflon-lined stainless steel autoclave for the hydrothermal treatment at 220 ℃ for 24 h. Finally, the as-prepared product, denoted as BTO, was washed with deionized water several times and dried at 60 ℃ for 12 h in a vacuum drying oven.

2.3 Synthesis of Nb-doping $Bi_4Ti_3O_{12}$ nanosheets

The series of Nb-doped $Bi_4Ti_3O_{12}$ nanosheets were synthesized by the same method as $Bi_4Ti_3O_{12}$ nanosheets. The details are as follows: Firstly, $Bi(NO_3)_3 \cdot 5H_2O$, TiO_2, Nb_2O_5, and NaOH were added into 30 mL of deionized water according to the composition of $Bi_4Nb_xTi_{3-x}O_{12}$ and stirred for 30 min at room temperature. Then, the above slurry was transferred to a Teflon-lined stainless steel autoclave for the hydrothermal treatment at 220 ℃ for 24 h. Finally, the products were obtained by adjusting the "*X*" to 0.01, 0.03, 0.05, and 0.07, denoted as BTO-0.01Nb, BTO-0.03Nb, BTO-0.05Nb, and BTO-0.07Nb in Section 3.

2.4 Characterizations

Phase compositions of the synthesized samples were characterized by an X-ray Diffractometer (XRD; Bruker AXS D8 Advance, Germany) with Cu Kα radiation (λ = 1.5418 Å), and their morphologies and elemental compositions were characterized by a high-resolution field emission scanning electron microscope (SEM; GeminiSEM 300, ZEISS, UK) and a high-resolution transmission electron microscope (HRTEM; Tecnai G2 F30 S-Twin TEM, FEI, USA). The specific surface area of all samples was analyzed via a BET analysis instrument (Beishide 3H-2000PS2, China). Optical properties of the samples were measured using a UV–Vis spectrometer (Cary 5000 Varian, Agilent, USA) with $BaSO_4$ as a reference. Element chemical states of the sample were investigated by an X-ray photoelectron spectroscope (XPS; ESCALAB 250 spectrometer, Thermo Scientific, USA). Active free radical signals were tested by an electron spin resonance (ESR) spectrometer (EMXPLUS, Bruker, Germany) using 5,5-dimethyl-l-pyrroline N-oxide (DMPO) as a trapping agent under simulated solar irradiation and ultrasonic vibration. CO_2 adsorption isotherms were carried out by a physical and chemical gas adsorption analyzer (Autosorb IQ, Quantachrome, USA). The open-circuit voltage and short-circuit charge were recorded by a high impedance electrometer (Keithley 6514, Tektronix, USA). A pressure control system was employed to apply vertical stress 20 N to samples with a diameter of 1-cm Cu foil as electrodes at a frequency of 1 Hz. The second-harmonic generation (SHG) measurement of the samples was tested by a modified Kurtz-Perry NLO system. The piezoelectricity including phase mapping,

butterfly curves, phase hysteresis loops, and surface potential of the samples were obtained using an AFM instrument (AFM; SPA-300HV, SEIKO, Japan). The powder samples were simply prepared into tablets by tablet press, and then fixed the tablet samples for the PFM and KPFM measurement.

2.5 Photocatalytic, piezocatalytic, and piezo-photocatalytic CO_2 reduction test

In a typical experiment, 10 mg of the powdered catalyst was suspended in 100 mL of deionized water. Then, the suspension was sealed in a custom-made glass reactor (300 mL) with a quartz glass top and purged with high purity CO_2 gas for 15 min to exclude other gases. Subsequently, the suspension was irradiated with a 300 W Xe lamp (Perfectlight, China) (15 cm between the lamp and the specimen) with an AM1.5G filter (100 mW·cm^{-2} in intensity) while maintaining the reactor temperature at 20 ℃. 1 mL of resultant gas was collected at regular intervals and analyzed by GC7920 gas chromatography device (Beijing China Education Au-light Co., Ltd., China) coupled with a thermal conductivity detector. 20 μL of liquid was injected into a gas chromatography device (GC9720 Plus, Fuli Instrument, China) to analyze liquid products. Piezo-catalytic CO_2 reduction experiment mainly differs from the photocatalytic CO_2 reduction process in that the reactor was submerged in an ultrasonicator (KQ-400DE 40 kHz, 260 W, Kunshan Ultrasonic Instruments Co., Ltd., China) without light irradiation. Similarly, the piezo-photocatalytic CO_2 reduction experiment combines the processes of both experiments in which the reactor was submerged in the ultrasonicator and irradiated with the Xe lamp. The ^{13}C isotope labeling experiment was analyzed by a mass spectrometer (GSD 350, OmniStar, Gemany) at room temperature with He as carrier gas. Also, the channel of reactant $^{13}CO_2$ (m/z = 45) and product ^{13}CO (m/z = 29) were monitored emphatically to filter out the reactant $^{13}CO_2$ and analyze dominant product ^{13}CO. High purity $^{13}CO_2$ (Wuhan Isotope Technology Co., Ltd., China) was used for the detection of carbon source.

2.6 Photocatalytic, piezocatalytic, and piezo-photocatalytic degradation test

Photocatalytic degradation experiments were measured in a 250 mL custom-made three-necked quartz flask reactor with a cooling water cycle to keep the reaction temperature of aqueous solution at 25±5 ℃. Specifically, 10 mg of the powdered catalyst was ultrasonically dispersed into 100 mL of RhB (100 mg·L^{-1}), followed by adsorption–desorption equilibrium at a speed of 100 r·min^{-1} between the catalyst and RhB in the dark for 45 min. At fixed irradiation intervals (300 W Xe lamp, 100 mW·cm^{-2} in intensity, with an AM1.5G filter, 15 cm between the lamp and the specimen), 3 mL of aliquot was removed from the suspension and centrifuged to remove any precipitate. Finally, the residual concentrations of organic pollutants were determined by measuring the absorbance at 553 nm using an UV–Vis photometer (UV-6100, Mapada, China). As for the piezo-catalytic degradation, the protocol was done using a three-necked quartz flask reactor submerged in an ultrasonicator (KQ-400DE 40 kHz, 260 W) without Xe lamp irradiation. Similarly, for the piezo-photocatalytic degradation experiment, the reactor was submerged in the ultrasonicator and exposed to a fixed irradiation interval by a 300 W Xe lamp with the same condition in the photocatalytic degradation experiment. In the piezo-photocatalytic degradation reaction process, the possible active species, like superoxide radical (•O_2^-), hydroxyl radicals (•OH), electrons (e^-), and holes (h^+) are investigated by adding L(+)-Ascorbic acid (LAA, 1 mM), isopropyl alcohol (IPA, 1 mM), $AgNO_3$ (1 mM), and ethylene diamine tetraacetic acid disodium salt (EDTA-2Na,1 mM), respectively.

2.7 Photoelectrochemical and piezoelectrochemical tests

Photocurrent response, piezo-current response, electrochemical impedance spectroscopy (EIS), and Mott–Schottky were carried out by an electrochemical workstation (CHI-760E, Chenhua Instruments Co., Ltd., China) with a standard three-electrode system under simulated solar light (300 W Xe lamp, 100 mW·cm^{-2} in intensity, with an AM1.5G filter, Perfectlight, China) or an ultrasonic irradiation (KQ-400DE 40 kHz, 260 W). The platinum (Pt) wire and saturated calomel electrode (SCE) were used as a counter electrode and a reference electrode, respectively, and 0.1 M Na_2SO_4 solution was used as an electrolyte. 10 mg of sample powders was uniformly fixed on an ITO glass substrate (2 cm × 4 cm) by conductive adhesive.

3 Results and discussion

3.1 Materials synthesis and characterizations

Crystal structures of BTO and BTO-XNb (where X = 0.01, 0.03, 0.05, and 0.07 relative amounts of Nb added) were analyzed by X-ray diffraction (XRD). Diffraction peaks of all samples matched well with the typical diffraction pattern of orthorhombic phase $Bi_4Ti_3O_{12}$ (JCPDS#35-0795) (Fig. 1(a)). In addition, no other diffraction peaks were observed, indicating that the Nb-doped samples still preserved the single-phase crystalline structure. Notably, the strongest diffraction peak (117) at ~30.1° displays a slight shift toward lower angles with increasing Nb doping (Fig. 1(b)), and we attribute this to the substitution of Ti^{4+} (0.61 Å) ions with relatively larger Nb^{5+} (0.64 Å) ions [50], which results in the expansion of the lattice. Similarly, the twin peaks at ~33° corresponding to the (200) and (020) planes shift slightly to become more deconvoluted with increasing Nb doping (Fig. 1(c)), suggesting the increase in orthorhombic distortion and enhanced polarity [51]. We further characterize the structure of the as-synthesized Nb-doped BTO nanosheets using Raman spectroscopy. Typically, the vibrational modes at 269, 325, 536, and 850 cm^{-1} can be associated with torsional bending vibrations, opposing excursion of external apical oxygen atoms and stretching vibrations of TiO_6 octahedron, respectively [52]. As the amount of Nb doping increases, we observe that these modes are visibly broadened with lowered intensities, suggesting that the Nb^{5+} ions are positioned at the B-sites in the perovskite layer, resulting in the lattice distortion (Fig. 1(d)). To further corroborate microscopic crystal structures of the samples, the lattice constants and unit-cell volumes were also simulated using Rietveld refinement of the XRD patterns using the GSAS software in the *B2cb* space group. The fitted curves of all samples are in close agreement with that of our experimental data, with good reliability factors (R_{wp} (7.82%–8.87%) and χ^2 (1.33–2.39)), thereby indicating that the results are of adequate reliability (Fig. S1 in the Electronic Supplementary Material (ESM)). Notably, as the amount of Nb doping increases, the cell volumes and orthorhombic distortion (b/c) values show a distinctive increase from BTO-0.01Nb to BTO-0.07Nb (Fig. 1(e) and Fig. S2 in the ESM), further confirming the above mentioned XRD results. Moreover, since there are three mono-octahedral layers within the $Bi_4Ti_3O_{12}$ structure, there are two octahedrally coordinated Ti^{4+} cations that are asymmetrically bonded to six oxygen atoms and hence two different possible

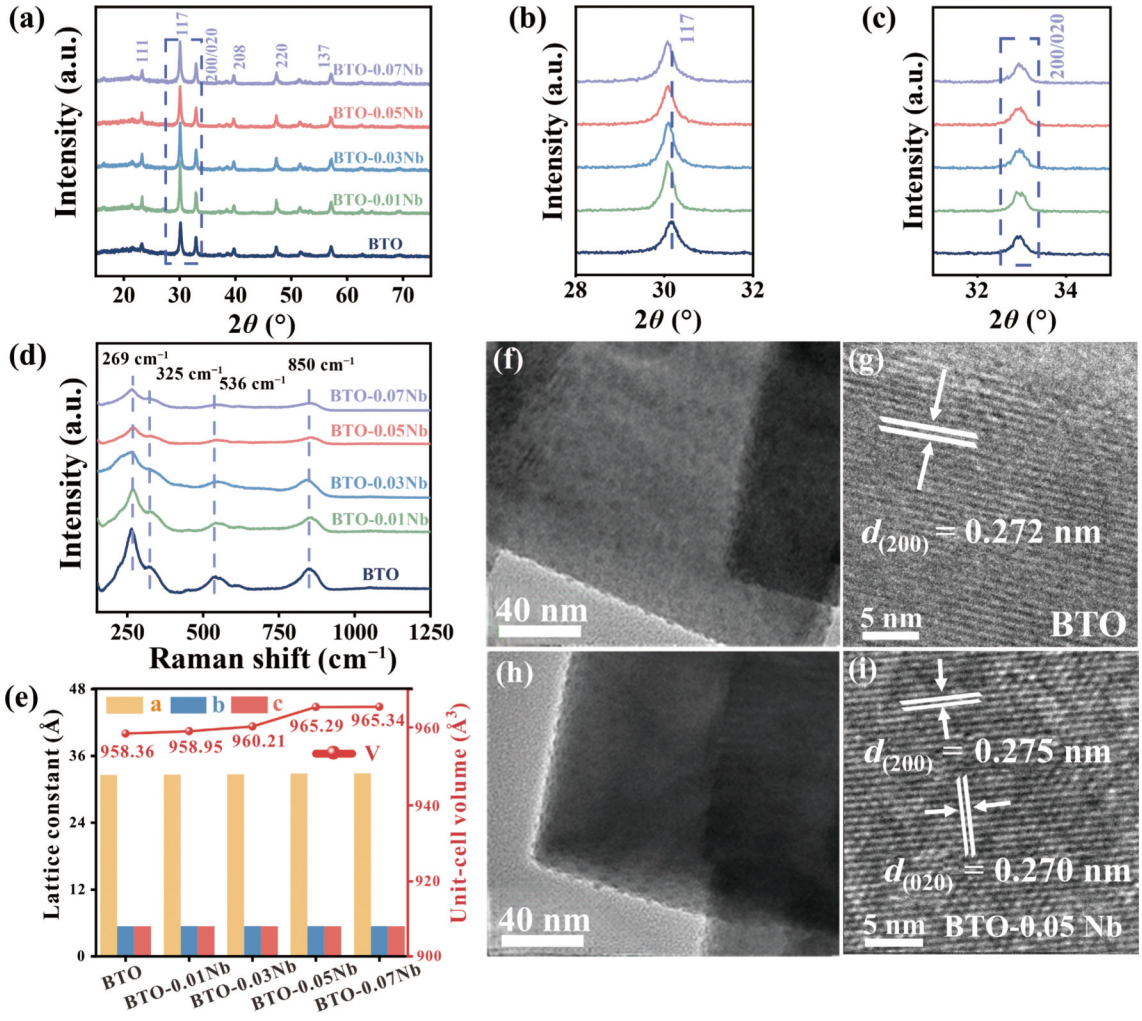

Fig. 1 (a) XRD patterns of BTO and BTO-*X*Nb (*X* = 0.01, 0.03, 0.05, and 0.07). (b, c) Enlarged XRD patterns of (117) peak and (200/020) peaks. (d) Raman spectra of BTO and BTO-*X*Nb (*X* = 0.01, 0.03, 0.05, and 0.07). (e) Lattice constants and unit-cell volumes of BTO and BTO-*X*Nb (*X* = 0.01, 0.03, 0.05, and 0.07). (f, g) TEM image and HRTEM image of BTO. (h, i) TEM image and HRTEM image of BTO-0.05Nb.

positions for Nb atoms to substitute (Fig. S3 in the ESM). Hence, we also calculate probability of each substitution through the Rietveld refinement of XRD patterns (Table S1 in the ESM).

Next, we characterize the morphology and crystalline structure of pristine BTO and our Nb-doped BTOs using scanning electron microscopy (SEM) and high-resolution transmission electron microscopy (HRTEM). All the samples including doped and pristine BTO appear to have a similar morphology and resemble nanoflowers made of an assembly of layered nanosheets (Fig. S4 in the ESM). The HRTEM images further suggest that the nanosheet structures (Figs. 1(f) and 1(h)), and their specific surface area is about 7–11.2 $m^2 \cdot g^{-1}$ (Fig. S5 in the ESM), indicating that the element doping process did not alter the microscopic morphology of BTO. In addition, the HRTEM images reveal that BTO-0.05Nb possesses two sets of perpendicular crystal lattices with the interplanar spacing of 0.275 and 0.270 nm that can be assigned to the (200) and (020) planes, respectively, while BTO has an interplanar spacing of 0.272 nm corresponding to the (200) plane (Figs. 1(g) and 1(i)). TEM energy dispersive X-ray (EDX) elemental mappings also affirm that there is a homogeneous distribution of Bi, Ti, Nb, and O elements across BTO and BTO-0.05Nb (Figs. S6 and S7 in the ESM), confirming that Nb was successfully incorporated into the B-sites of the perovskite layer of BTO.

3.2 Electronic structure and optical properties

Subsequently, we investigate electronic and optical properties of our Nb-doped BTO nanosheets. Optical properties of BTO and BTO-*X*Nb are measured using UV–vis diffuse reflectance spectroscopy (DRS). Photo-absorption and band energy edge of the as-obtained samples display no visible difference compared with pristine BTO, indicating that the low concentration of Nb doping causes minimal change to the energy band position (Fig. 2(a), Figs. S8–S11 in the ESM). Using BTO-0.05Nb as a representative doped sample, the surface composition and chemical states of the related elements are investigated using XPS. Bi, Ti, and O, are present in both BTO and BTO-0.05Nb, while Nb is only present in BTO-0.05Nb, further affirming the successful doping of Nb into BTO (Figs. 2(b) and 2(c)). Further investigation of the Bi $4f_{5/2}$ and Bi $4f_{7/2}$ peaks at ~158.7 and 164.1 eV, respectively, reveals that the binding energy of Bi 4f of BTO-0.05Nb is slightly shifted to lower energy compared to BTO, and we attribute this to the donor doping effect of Nb (Fig. 2(d)). In addition, the binding energy of Ti 2p for BTO and BTO-0.05Nb are at about 458.0 and 464.2 eV, respectively. The peaks at 457.7 and 462.0 eV can be attributed to the Ti^{3+} cation in which the valence of some Ti ions are converted from +4 to +3 to maintain electroneutrality (Fig. 2(e)) [53]. The O 1 s XPS spectra reveal the existence of lattice oxygen (~529.7 eV) while the stronger peaks at

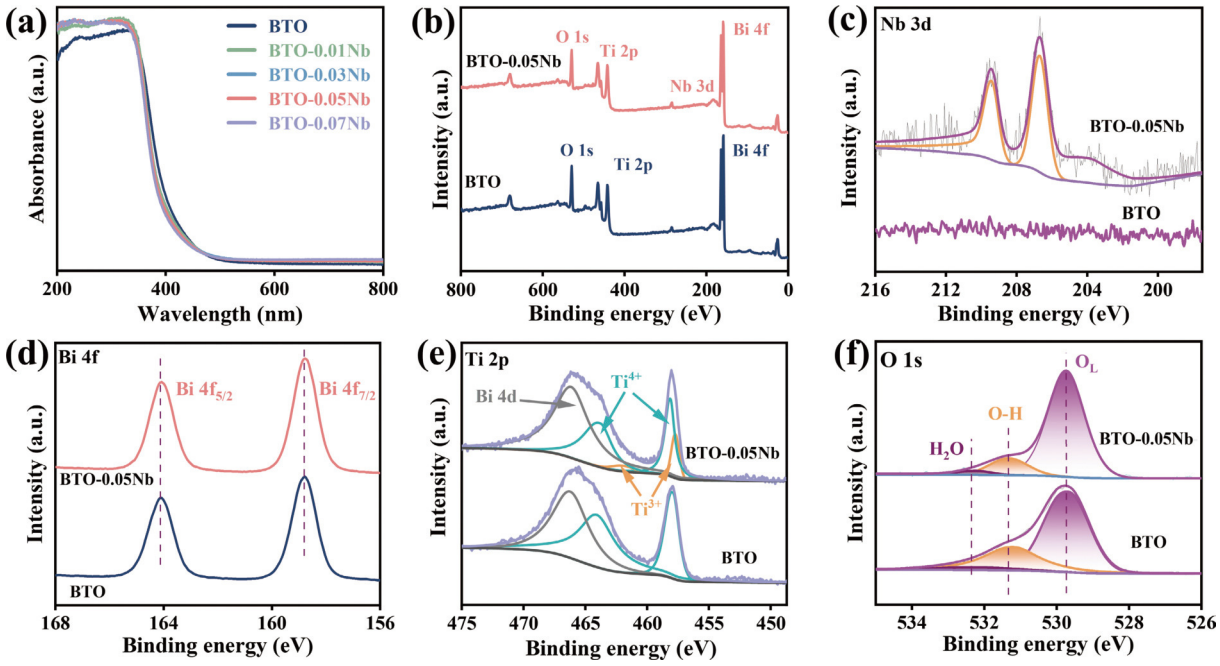

Fig. 2 (a) UV–vis diffuse reflectance spectra of BTO and BTO-*X*Nb (X = 0.01, 0.03, 0.05, and 0.07). XPS spectra of (b) survey scan, (c) Nb 3d, (d) Bi 4f, (e) Ti 2p, and (f) O 1s of BTO and BTO-0.05Nb.

531.3 and 532.4 eV are assigned to surface hydroxyls and adsorbed water on the BTO surface (Fig. 2(f)). Compared to BTO, there is a decrease in the oxygen vacancy after Nb doping, which further verifies by electron paramagnetic resonance (EPR) analysis (Fig. S12 in the ESM).

3.3 CO_2 reduction performance

Because BTO is uniquely both photocatalytic and piezoelectric active, we investigate carbon dioxide (CO_2) reduction catalytic performance of Nb-doped BTO nanosheets by simulated solar irradiation, ultrasonic vibration, and synergistic ultrasonic vibration under light conditions without the presence of cocatalysts or sacrificial agents. Firstly, we ascertain the photocatalytic CO_2 reduction performance of our nanostructures via the illumination of simulated solar light. In brief, we introduce CO_2 into a reactor containing a suspension of BTO-*X*Nb and irradiate the reactor with an Xe lamp. All samples generate carbon monoxide (CO) and hydrogen (H_2) as the dominant reductive product. Notably, BTO-0.05Nb achieved the highest CO and H_2 evolution rates of 2.63 and 0.74 μmol·g^{-1}·h^{-1}, more than ~1.64 and 1.61 times better than that of BTO (1.60 and 0.46 μmol·g^{-1}·h^{-1}) (Figs. 3(a) and 3(b), Figs. S13(a) and S13(b) in the ESM). Moreover, all other Nb-doped BTO samples also show remarkable improvement of the CO and H_2 yield rate compared to pristine BTO. We further compare the piezocatalytic performance of BTO-*X*Nb by subjecting the reactor to ultrasonic vibration. Similar to the photocatalytic reaction, CO and H_2 can also be detected in all samples, with BTO-0.05Nb achieving the highest CO and H_2 evolution rates of 19.58 and 8.57 μmol·g^{-1}·h^{-1} (Figs. 3(c) and 3(d), Figs. S13(c) and S13(d) in the ESM), ~5.19 and 2.76 times faster than that of BTO (3.77 and 3.10 μmol·g^{-1}·h^{-1}). Subsequently, we choose BTO-0.05Nb as the representative Nb-doped sample to further evaluate the piezo-photocatalytic performance, and CO_2 reduction experiments are carried out under both simulated solar irradiation and ultrasonic vibration. Remarkably, the CO and H_2 production rates of BTO-0.05Nb increased to 72.70 and 18.93 μmol·g^{-1}·h^{-1}, respectively, which are over ~4.69 and 2.28 times than that of BTO (15.50 and 8.29 μmol·g^{-1}·h^{-1}), outperforming most piezo-photocatalysts reported to date (Table S2 in the ESM). The production rates of CO and H_2 significantly surpasses the combined rate achieved under light irradiation alone and ultrasonic vibration alone (denoted as BTO-0.05Nb (U+L)), which measured at 22.21 and 9.31 μmol·g^{-1}·h^{-1}, respectively, (Figs. 3(e) and 3(f), Figs. S13(e) and S13(f) in the ESM). This result strongly implies the occurrence of an enhanced synergistic piezo-photocatalytic effect, attributed to the macroscopic polarization enhancement of BTO-0.05Nb (to be discussed in Section 3.5). Besides, BTO-0.05Nb presents high durability with negligible activity decay after six consecutive cycles (Fig. S14 in the ESM). On the contrary, when control experiments were conducted under argon (Ar) atmosphere instead of CO_2 purging, no detectable CO was observed. This confirms that observed CO emissions from previous experiments are a result of the catalytic conversion of CO_2 and not due to carbon contaminants (Fig. S15 in the ESM). Additional control experiments conducted in the absence of light, ultrasonic vibration or without the presence of BTO catalysts also yielded no CO production. This underscores that the CO generation is attributed to the photocatalytic and/or piezocatalytic effects of the BTO nanosheets. In addition, we further verify that the CO product is indeed arising from the CO_2 reduction by substituting the CO_2 source with $^{13}CO_2$. From the mass spectroscopy data, the distinct peak at m/z = 29 corresponds to ^{13}CO while the peak at m/z = 45 corresponds to the unreacted $^{13}CO_2$. Hence, this unequivocally confirms that the origin of CO is, in fact, due to the conversion of CO_2 and not the presence of carbon contaminants (Fig. 3(f)).

3.4 Degradation RhB performance

To further highlight the piezo-photocatalytic activity of our Nb-doped BTO nanosheets, we examine the catalytic degradation performance using rhodamine B (RhB) as model organic pollutant. When the reactor is subjected to light irradiation and ultrasonic vibration without any catalyst, there is almost no RhB

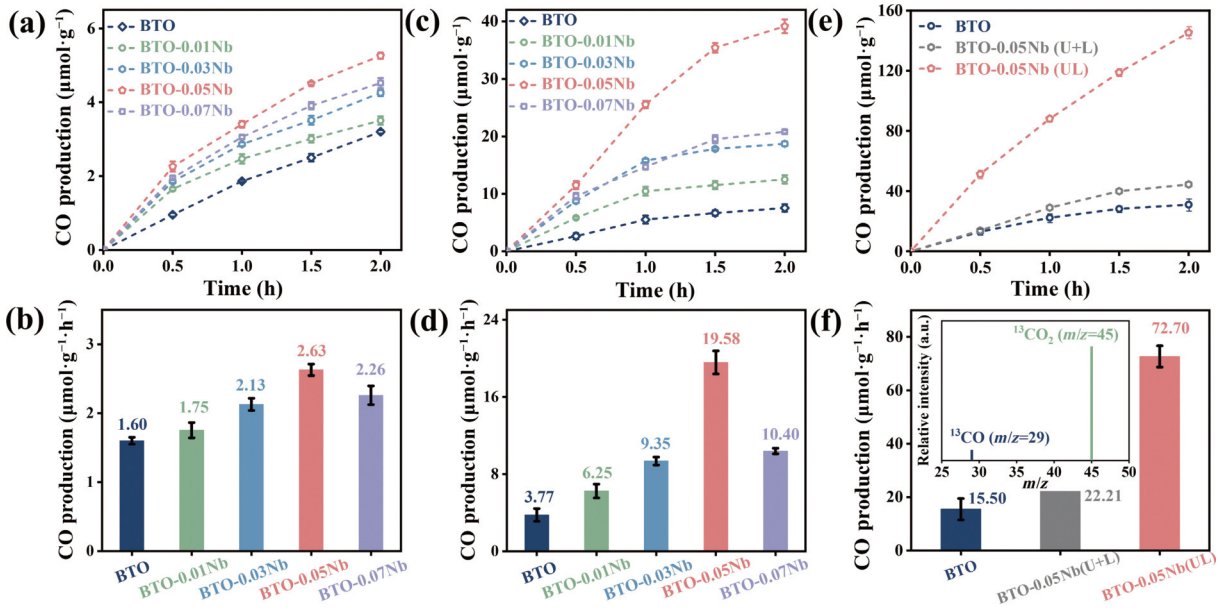

Fig. 3 (a) CO production yield and (b) corresponding CO production rates of BTO and BTO-*X*Nb (X = 0.01, 0.03, 0.05, and 0.07) under simulated solar light. (c) CO production yield and (d) corresponding CO production rates of BTO and BTO-*X*Nb (X = 0.01, 0.03, 0.05, and 0.07) under ultrasonic vibration. (e) CO production yield and (f) corresponding CO production rates of BTO and BTO-0.05Nb under simulated solar light and ultrasonic vibration (inset of (f): mass spectra for CO_2 reduction of BTO-0.05Nb with using $^{13}CO_2$ as reacting gas). BTO-0.05Nb (U+L) represents sum of catalytic performance of BTO-0.05Nb under light irradiation alone and ultrasonic vibration alone, and BTO-0.05Nb (UL) represents synergistic catalytic performance of BTO-0.05Nb under light irradiation and ultrasonic vibration.

degradation (Fig. S16 in the ESM). In addition, we also establish that the catalyst achieves adsorption–desorption equilibrium in dark within 45 min (Fig. 4(a)). When subjected to the ultrasonic vibration, all the BTO-*X*Nb nanosheets present enhanced piezocatalytic activity compared to that of pristine BTO. Notably, BTO-0.05Nb possesses the highest piezocatalytic activity reaching ~91.2% RhB degradation in 90 min with a rate constant (k) of 0.0242 min^{-1}. In contrast, BTO presents weaker piezocatalytic performance with degradation efficiencies of ~37.8% in 90 min, while the piezocatalytic rate constant (k) is 0.0051 min^{-1}, again underlining that BTO-0.05Nb possesses excellent piezoelectric property (Figs. 4(a) and 4(b), Figs. S17 and S18 in the ESM). On the other hand, both BTO and BTO-0.05Nb display poor photocatalytic activity with inefficient RhB degradation (Fig. S19 in the ESM), likely due to the high RhB concentration (100 $mg·L^{-1}$). Importantly, when subjected to both ultrasonic vibration and light irradiation, BTO-0.05Nb achieves synergistically enhanced piezo-photocatalytic performance corresponding to over ~94% RhB degradation in 60 min with a rate constant (k) of 0.0493 min^{-1}, which is ~3.39 times higher than that of BTO (Figs. 4(c) and 4(d), Fig. S20 in the ESM). Remarkably, these results also outperform most of the reported catalysts under similar testing conditions (Table S3 in the ESM). In addition, all other Nb-doped BTO samples also show remarkable synergistically improved piezo-photocatalytic RhB degradation performance compared to pristine BTO (Fig. S21 in the ESM). The removal amounts of total organic carbon (TOC) of all samples well match their degradation performance (Fig. S22 in the ESM), revealing that most RhB molecules are mineralized after the piezo-photocatalytic reaction process by BTO-0.05Nb. We further examine the superior performance of our BTO-0.05Nb nanosheets over a range of RhB concentrations from 5 to 500 $mg·L^{-1}$. Significantly, the BTO-0.05Nb demonstrates an exceptionally-high piezo-photocatalytic degradation rate at low concentrations of RhB and maintains remarkable piezo-photocatalytic activity even at high concentrations of RhB. Within 300 s, RhB solution (5 $mg·L^{-1}$) can be degraded by more than 90% in the presence of BTO-0.05Nb. Furthermore, high concentrations of RhB (300 and 500 $mg·L^{-1}$) were degraded entirely within 150 and 300 min, respectively (Fig. 4(e) and Fig. S23 in the ESM). In addition to RhB, BTO-0.05Nb also shows excellent piezo-photocatalytic performance compared to MB, MO, TC, and BPA removal efficiency reach ~100%, ~87%, ~90%, and ~90% within 90 min (Fig. S24 in the ESM), respectively, demonstrating potentiality and versatility for the treatment of complex pollutant. Notably, our BTO-0.05Nb nanosheets possess high durability and recyclability, showcasing negligible activity decay even after six consecutive cycles (Fig. 4(f), Figs. S25 and S26 in the ESM). To explore the role of the primary active species in the piezo-photodegradation process, L(+)-ascorbic acid (LAA), isopropyl alcohol (IPA), $AgNO_3$, and disodium ethylene diamine tetraacetic acid disodium salt (EDTA-2Na) are employed as scavengers of $•O_2^-$, •OH, e^-, and h^+ respectively, to analyze degradation mechanisms. The RhB degradation efficiency was slightly inhibited in the presence of EDTA-2Na, $AgNO_3$, and LLA (Figs. 4(g) and 4(h)). In contrast, the degradation rate of RhB decreased significantly after the addition of IPA, indicating that •OH is the dominant reactive species in the piezo-photocatalytic process. The generation of reactive oxygen species (ROS) was further determined by electron spin-resonance (ESR) technique. As illustrated in Fig. 4(i) and Fig. S27 in the ESM, the characteristic signals of •OH for BTO-0.05Nb were much higher when compared to BTO, further suggesting that •OH plays a significant role as dominant reactive species.

3.5 Enhanced macroscopic polarization promoting charge separation

Lastly, we delve into the mechanism behind the enhanced and synergistic piezo-photocatalytic performance exhibited by our BTO-*X*Nb nanosheets to offer valuable insights into the design of nanocatalysts. It has been reported that ion substitution is an effective strategy to increase the local dipole moments which is caused by enhancing the structural distortion degree, and

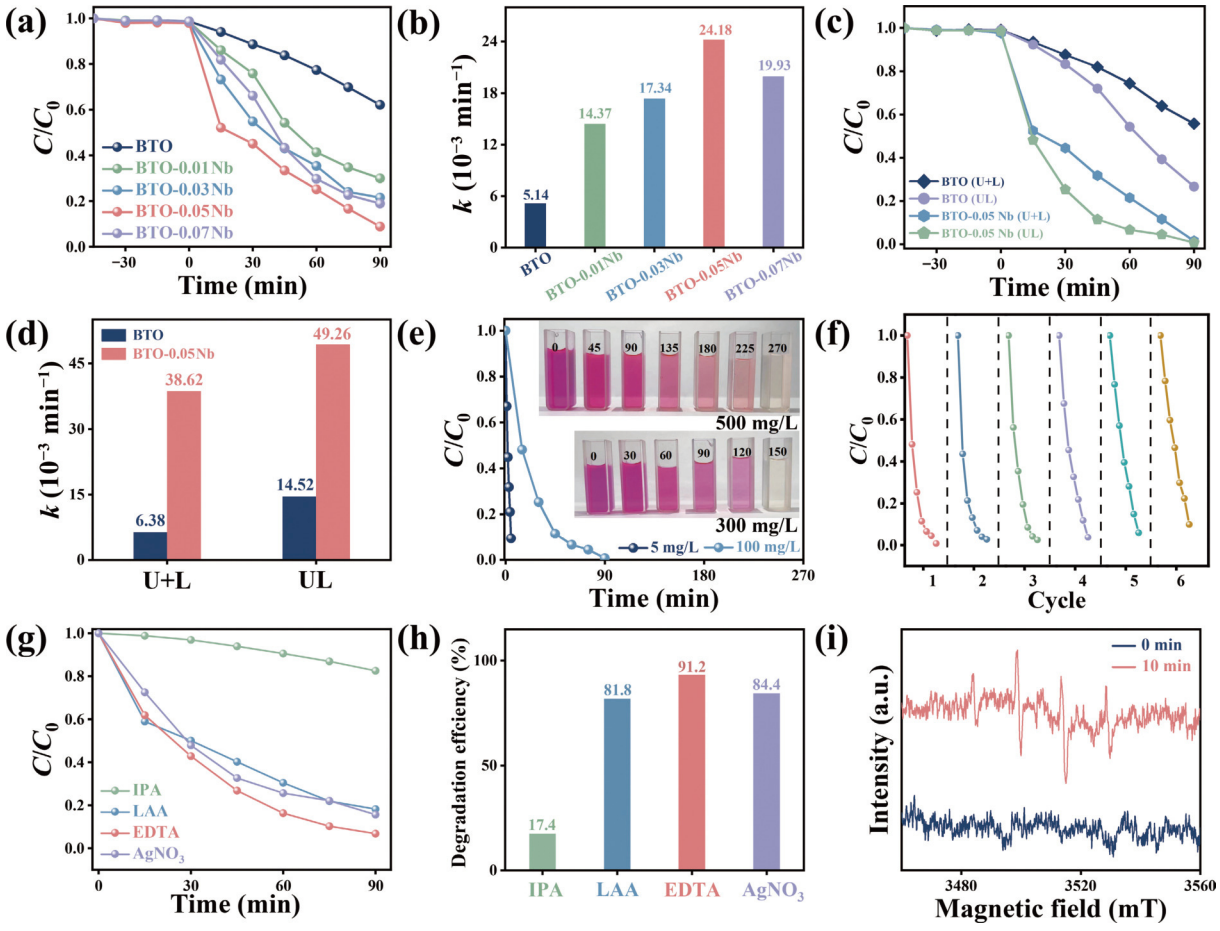

Fig. 4 (a, b) Adsorption and piezo-degradation curves of RhB and corresponding first-order reaction kinetic constants (k) for BTO and BTO-XNb (X = 0.01, 0.03, 0.05, and 0.07) under ultrasonic vibration. (c, d) Adsorption and piezo-photodegradation curves of RhB and corresponding first-order reaction kinetic constants (k) for BTO and BTO-0.05Nb under simulated solar light and ultrasonic vibration. Here, U+L represents sum of catalytic performance of BTO and BTO-0.05Nb under light irradiation alone and ultrasonic vibration alone, and UL represents synergistic catalytic performance of BTO and BTO-0.05Nb under light irradiation and ultrasonic vibration. (e) Piezo-photodegradation of different concentrations of RhB over BTO-0.05Nb under simulated solar light and ultrasonic vibration. (f) Piezo-photodegradation of RhB over 6 reaction cycles when using BTO-0.05Nb. (g, h) Piezo-photodegradation curves and corresponding efficiencies of RhB using BTO-0.05Nb with addition of scavengers. (i) ESR spin-trapping of BTO-0.05Nb with DMPO for identification of •OH radicals.

ultimately improving macroscopic polarization [54]. We employ piezo-response force microscopy (PFM) to investigate and verify the piezoelectric property of BTO and BTO-0.05Nb. The morphology and phase images show clear contrast in BTO-0.05Nb, highlighting the different polarization orientations (Figs. 5(a) and 5(b)). Both BTO and BTO-0.05Nb present typical response of ferroelectric effect with ~180° phase alterations, suggesting the polarization switchable process in two samples (Figs. 5(c) and 5(d)). Moreover, the butterfly amplitude loop of BTO and BTO-0.05Nb further confirms their effectual piezoelectric response (Figs. 5(c) and 5(d)). It can be observed that the maximum amplitude of BTO-0.05Nb is significantly steeper and greater than that of pristine BTO, implying that BTO-0.05Nb exhibits higher maximum effective piezoelectric coefficient (d_{33}) and stronger piezoelectric polarization. The surface potential of BTO and BTO-0.05Nb was also monitored by Kelvin probe force microscopy (SKPFM). There is an apparent difference in the surface potential distribution between bright and dark regions, with BTO-0.05Nb displaying a higher surface charge potential (~80 mV) than that of BTO (~40.6 mV) (Figs. 5(g)–5(i)). These results therefore strongly suggest that the Nb doping can significantly improve the ferroelectric spontaneous polarization and piezoelectric response of BTO, which in turn effectively induce charge migration. Moreover, we utilize second-harmonic generation (SHG) to further confirm the macroscopic polarity difference between BTO and BTO-0.05Nb. BTO-0.05Nb exhibits a superior SHG response of ~1.64 times higher that of BTO, corroborating that the Nb doping of BTO can effectively amplify macroscopic polarity (Fig. 5(e)) [55]. As a result of the notable enhancement in macroscopic polarization, BTO-0.05Nb demonstrates the highest CO_2 adsorption capacity which then facilitates the catalytic reduction of CO_2 (Fig. 5(f)).

To verify the relationship between efficient charge transfer separation and macroscopic polarization enhancement, electrochemical tests of piezo-, photocurrent, and electrochemical impedance spectroscopy (EIS) Nyquist plots are conducted. BTO-0.05Nb exhibits a higher photocurrent response and smallest arc radius, owing to the polarization enhancement induced by element doping and donor doping effect of Nb. Thus, this leads to lower interfacial resistance and higher charge separation efficiency (Figs. 6(a) and 6(b)). Similarly, BTO-0.05 Nb showcases the highest current density and significantly reduced charge transfer resistance when subjected to ultrasonic vibration, indicating that the migration of increased piezoelectric electrons is accelerated by the enhanced piezoelectric field (Figs. 6(c) and 6(d)). In addition, BTO-0.05Nb presents higher open-circuit voltage and short-circuit charge compared to BTO under 20 N (Figs. 6(e) and 6(f)), further suggesting that a stronger piezoelectric field is realized in

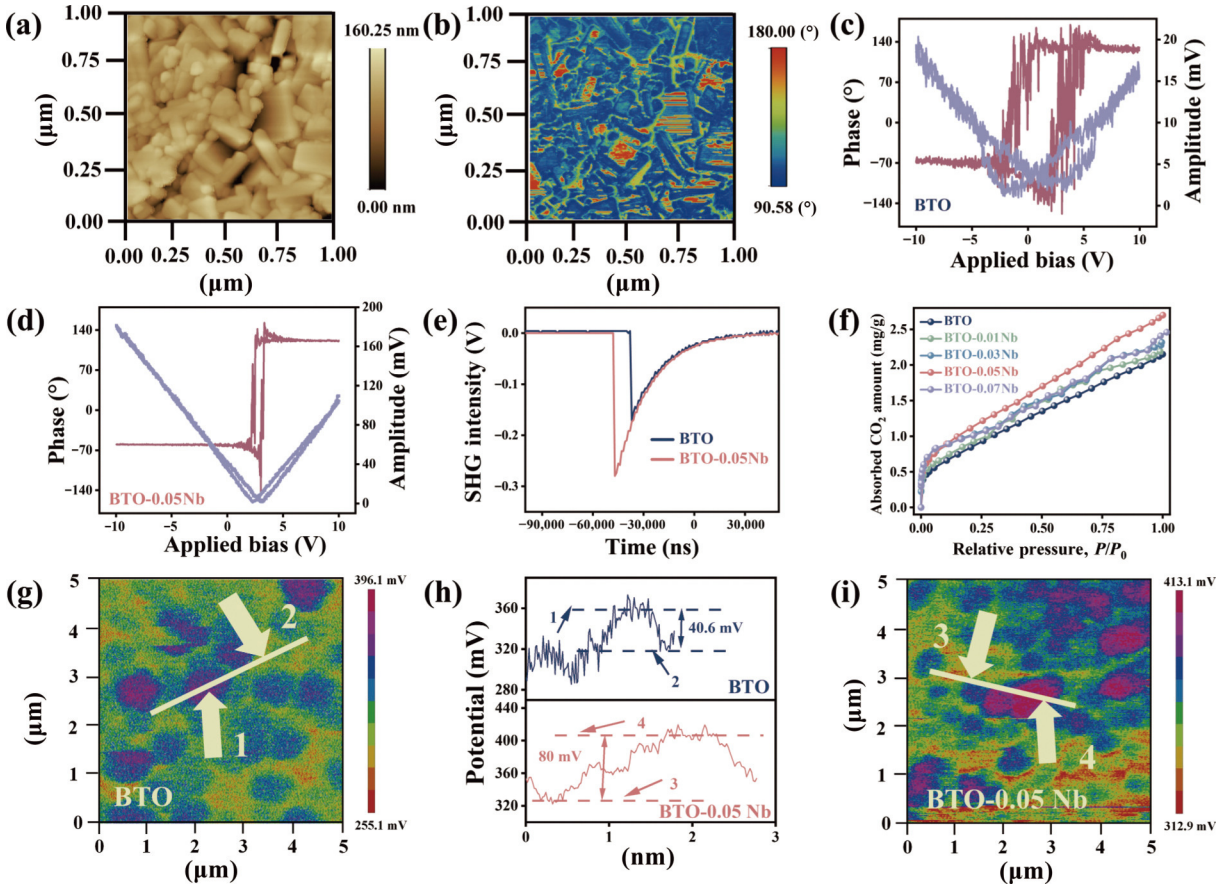

Fig. 5 (a) AFM image of BTO-0.05Nb. (b) PFM phase mapping of BTO-0.05Nb. (c, d) Butterfly curves and phase hysteresis loops of BTO and BTO-0.05Nb. (e) SHG generation for BTO and BTO-0.05Nb. (f) CO_2 adsorption isotherms of BTO and BTO-*X*Nb (*X* = 0.01, 0.03, 0.05, and 0.07). (g, i) Surface charge and (h) corresponding charge difference profile of BTO and BTO-0.05Nb.

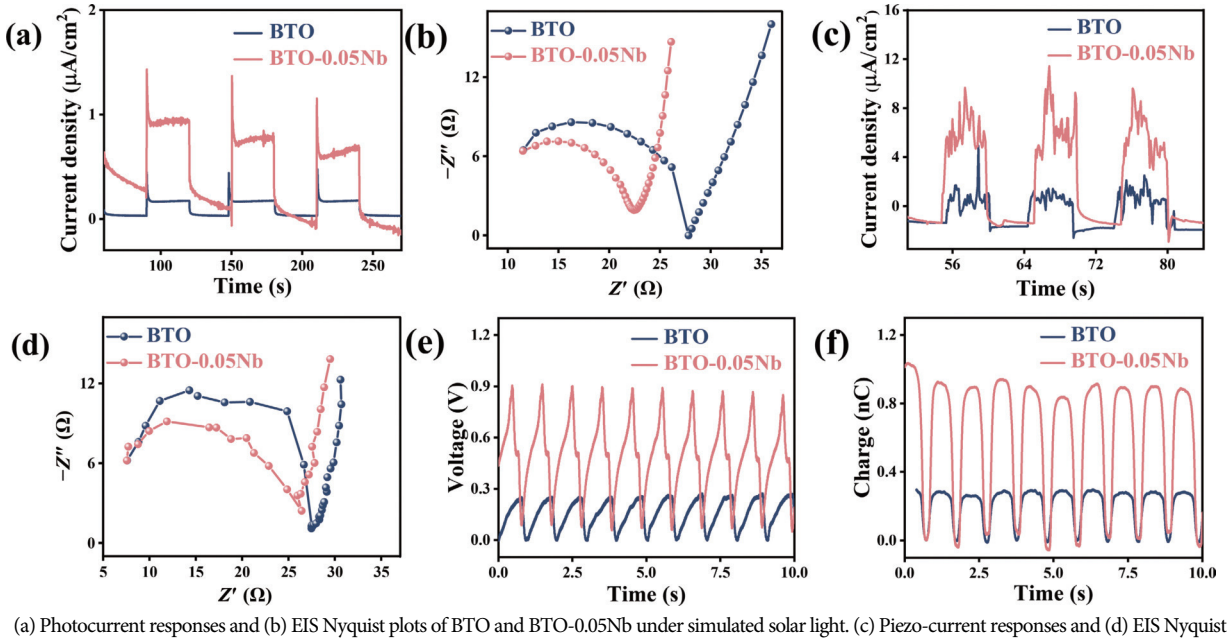

Fig. 6 (a) Photocurrent responses and (b) EIS Nyquist plots of BTO and BTO-0.05Nb under simulated solar light. (c) Piezo-current responses and (d) EIS Nyquist plots of BTO and BTO-0.05Nb under ultrasonic vibration. (e) Open-circuit voltage and (f) short-circuit charge of BTO and BTO-0.05Nb.

BTO-0.05Nb. Consequently, the stronger piezoelectric field promotes the separation of photogenerated electrons and holes.

According to all the above experimental results and analysis, a possible mechanism for piezo-photocatalytic CO_2 reduction and pollutant degradation process was proposed (Fig. S28 in the ESM). BTO-0.05Nb owns an enhanced macroscopic polarization and increasing charge carrier concentration achieved via Nb doping, resulting in larger band bending with a stronger potential difference. When applying a periodic stress generated by the ultrasonic vibration, BTO-0.05Nb could induce a desirable piezoelectric field across the whole bulk, which triggers the tilting of energy bands. This significantly enhanced piezoelectric field can

effectively boost the separation and directed migration of photo-induced carriers as the simultaneous action of light and ultrasound. As a result, the accumulated electrons and holes on the opposite surfaces of BTO-0.05Nb are involved in the redox reactions, promoting the adsorption and activation of CO_2 and generation of highly active •OH radicals, which jointly advance the catalytic performance for CO_2 reduction and degradations of organic pollutant. Notably, the strong piezoelectric field induced by enhanced macroscopic polarization plays an extremely significant role, further affirming the element doping strategy is an approach to construct high-activity piezo-photocatalytic systems. Therefore, this work provides valuable insights toward the rational design and facile fabrication of next-generation, high-performance, and multi-responsive catalysts for diverse applications such as energy conversion, environmental conservation, and chemical reactions.

4 Conclusions

In summary, we have successfully fabricated a series of Nb-doping BTO nanocatalysts via a facile one-step hydrothermal method. When compared with unmodified $Bi_4Ti_3O_{12}$, our optimized doped $Bi_4Ti_3O_{12}$ exhibits a remarkable enhancement in its piezo-photocatalytic performance for CO_2 reduction. Notably it achieves a high CO production rate of 72.7 $\mu mol \cdot g^{-1} \cdot h^{-1}$ without the need of any cocatalyst or sacrifice agent. Besides CO_2 reduction, our piezo-photocatalytic degradation tests also reveal that the optimized BTO-0.05Nb nanocatalyst outperforms at various pollutant concentration levels. The mechanisms underpinning this synergistic enhancement in piezo-photocatalytic activity can be attributed to the macroscopic polarization enhancement resulting from lattice distortion and an increase in lattice constants induced by optimal niobium doping. These effects consequently contribute to a substantial improvement in the photoinduced charge separation efficiency. In conclusion, our work provides a promising and effective approach for the development of a new generation of high-performance catalysts that are driven by both solar and mechanical energy. These catalysts hold great potential for applications in energy conversion and environmental remediation.

Acknowledgements

The authors gratefully acknowledge financial support from the Natural Science Foundation of Jiangsu Province (No. BK20220596), Innovative Science and Technology Platform Project of Cooperation between Yangzhou City and Yangzhou University, China (No. YZ202026305), the Natural Science Foundation of China (Nos. 21922202 and 21673202), the Priority Academic Program Development of Jiangsu Higher Education Institutions, Shaanxi Province High-level Talent Introduction Program (Youth Project), Doctoral Research Start-up Fund project of Xi'an Polytechnic University (No. 107020589), the Biological Resources Development and the Textile Wastewater Treatment Innovation Team (No. 23JP055). We would also like to acknowledge the technical support received at the Testing Center of Yangzhou University.

Declaration of competing interest

The authors have no competing interests to declare that are relevant to the content of this article.

Electronic Supplementary Material

Supplementary material is available in the online version of this article at https://doi.org/10.26599/JAC.2024.9220866.

References

[1] Xu CP, Ravi Anusuyadevi P, Aymonier C, *et al.* Nanostructured materials for photocatalysis. *Chem Soc Rev* 2019, **48**: 3868–3902.
[2] Candish L, Collins KD, Cook GC, *et al.* Photocatalysis in the life science industry. *Chem Rev* 2022, **122**: 2907–2980.
[3] Guo Q, Ma ZB, Zhou CY, *et al.* Single molecule photocatalysis on TiO_2 surfaces. *Chem Rev* 2019, **119**: 11020–11041.
[4] Cao JZ, Xu ZM, Chen Y, *et al.* Tailoring the asymmetric structure of NH_2-UiO-66 metal-organic frameworks for light-promoted selective and efficient gold extraction and separation. *Angew Chem Int Ed* 2023, **62**: e202302202.
[5] Chen X, Guan SH, Zhou JJ, *et al.* Photocatalytic free radical-controlled synthesis of high-performance single-atom catalysts. *Angew Chem Int Ed* 2023, **62**: e202312734.
[6] Li XY, Wang C, Tang JW. Methane transformation by photocatalysis. *Nat Rev Mater* 2022, **7**: 617–632.
[7] Zou YQ, Hörmann FM, Bach T. Iminium and enamine catalysis in enantioselective photochemical reactions. *Chem Soc Rev* 2018, **47**: 278–290.
[8] Mai W, Wen F, Xie D, *et al.* Structure and composition study of carbon-doped titanium oxide film combined with first principles. *J Adv Ceram* 2014, **3**: 49–55.
[9] Li J, Cai LJ, Shang J, *et al.* Giant enhancement of internal electric field boosting bulk charge separation for photocatalysis. *Adv Mater* 2016, **28**: 4059–4064.
[10] Chen Y, Xu MJ, Wen JY, *et al.* Selective recovery of precious metals through photocatalysis. *Nat Sustain* 2021, **4**: 618–626.
[11] Chen Y, Guan SH, Ge H, *et al.* Photocatalytic dissolution of precious metals by TiO_2 through photogenerated free radicals. *Angew Chem Int Ed* 2022, **61**: e202213640.
[12] Zhang L, Xie ZX, Gong JL. Shape-controlled synthesis of Au–Pd bimetallic nanocrystals for catalytic applications. *Chem Soc Rev* 2016, **45**: 3916–3934.
[13] Jing JF, Yang J, Li WL, *et al.* Construction of interfacial electric field via dual-porphyrin heterostructure boosting photocatalytic hydrogen evolution. *Adv Mater* 2022, **34**: 2106807.
[14] Wu J, Li XD, Shi W, *et al.* Efficient visible-light-driven CO_2 reduction mediated by defect-engineered BiOBr atomic layers. *Angew Chem Int Ed* 2018, **57**: 8719–8723.
[15] Zhang A, Liu ZY, Xie B, *et al.* Vibration catalysis of eco-friendly $Na_{0.5}K_{0.5}NbO_3$–based piezoelectric: An efficient phase boundary catalyst. *Appl Catal B Environ* 2020, **279**: 119353.
[16] Wang ZL, Song JH. Piezoelectric nanogenerators based on zinc oxide nanowire arrays. *Science* 2006, **312**: 242–246.
[17] Park DS, Hadad M, Riemer LM, *et al.* Induced giant piezoelectricity in centrosymmetric oxides. *Science* 2022, **375**: 653–657.
[18] You YM, Liao WQ, Zhao DW, *et al.* An organic-inorganic perovskite ferroelectric with large piezoelectric response. *Science* 2017, **357**: 306–309.
[19] Tian WR, Li NJ, Chen DY, *et al.* Vibration-driven reduction of CO_2 to acetate with 100% selectivity by SnS nanobelt piezocatalysts. *Angew Chem Int Ed* 2023, **62**: e202306964.
[20] Zhang MX, Tao HC, Zhai CY, *et al.* Twin-brush ZnO mesocrystal for the piezo-activation of peroxymonosulfate to remove ibuprofen in water: Performance and mechanism. *Appl Catal B Environ* 2023, **326**: 122399.
[21] Shen PF, Yin P, Zou YT, *et al.* Ultra-fast piezocatalysts enabled by interfacial interaction of reduced graphene oxide/MoS_2 heterostructures. *Adv Mater* 2023, **35**: 2212172.
[22] Hu C, Hu JC, Zhu ZJ, *et al.* Orthogonal charge transfer by precise positioning of silver single atoms and clusters on carbon nitride for efficient piezocatalytic pure water splitting. *Angew Chem Int Ed* 2022, **61**: e202212397.
[23] Li M, Sun JX, Chen G, *et al.* Construction double electric field of sulphur vacancies as medium ZnS/Bi_2S_3–PVDF self-supported recover-

able piezoelectric film photocatalyst for enhanced photocatalytic performance. *Appl Catal B Environ* 2022, **301**: 120792.
[24] Liu ZR, Yu X, Li LL. Piezopotential augmented photo- and photo–electro-catalysis with a built-in electric field. *Chin J Catal* 2020, **41**: 534–549.
[25] Sudrajat H, Rossetti I, Colmenares JC. Piezocatalysis: A promising alternative route for CO_2 reduction. *J Mater Chem A* 2023, **11**: 24566–24590.
[26] Ren ZR, Chen F, Zhao Q, *et al.* Efficient CO_2 reduction to reveal the piezocatalytic mechanism: From displacement current to active sites. *Appl Catal B Environ* 2023, **320**: 122007.
[27] Phuong PTT, Vo DVN, Duy NPH, *et al.* Piezoelectric catalysis for efficient reduction of CO_2 using lead-free ferroelectric particulates. *Nano Energy* 2022, **95**: 107032.
[28] Li S, Zhao ZC, Li JB, *et al.* Mechanically induced highly efficient hydrogen evolution from water over piezoelectric SnSe nanosheets. *Small* 2022, **18**: 2202507.
[29] Pan L, Sun SC, Chen Y, *et al.* Advances in piezo-phototronic effect enhanced photocatalysis and photoelectrocatalysis. *Adv Energy Mater* 2020, **10**: 2000214.
[30] Jiang ZY, Tan XJ, Huang YX. Piezoelectric effect enhanced photocatalysis in environmental remediation: State-of-the-art techniques and future scenarios. *Sci Total Environ* 2022, **806**: 150924.
[31] Kang YY, Qi HZ, Wan GD, *et al.* Ferroelectric polarization enabled spatially selective adsorption of redox mediators to promote *Z*-scheme photocatalytic overall water splitting. *Joule* 2022, **6**: 1876–1886.
[32] Liu Y, Zhang MJ, Wang Z, *et al.* Bipolar charge collecting structure enables overall water splitting on ferroelectric photocatalysts. *Nat Commun* 2022, **13**: 4245.
[33] Li S, Zhao ZC, Liu MS, *et al.* Remarkably enhanced photocatalytic performance of Au/$AgNbO_3$ heterostructures by coupling piezotronic with plasmonic effects. *Nano Energy* 2022, **95**: 107031.
[34] Wang YJ, Li X, Chen YK, *et al.* Pulsed-laser-triggered piezoelectric photocatalytic CO_2 reduction over tetragonal $BaTiO_3$ nanocubes. *Adv Mater* 2023, **35**: 2305257.
[35] Su R, Shen YJ, Li LL, *et al.* Silver-modified nanosized ferroelectrics as a novel photocatalyst. *Small* 2015, **11**: 202–207.
[36] Singh S, Khare N. Coupling of piezoelectric, semiconducting and photoexcitation properties in $NaNbO_3$ nanostructures for controlling electrical transport: Realizing an efficient piezo-photoanode and piezo-photocatalyst. *Nano Energy* 2017, **38**: 335–341.
[37] Jiang YW, Li MZ, Mi Y, *et al.* The influence of piezoelectric effect on the heterogeneous photocatalytic hydrogen production of strontium titanate nanoparticles. *Nano Energy* 2021, **85**: 105949.
[38] Lan SY, Yu C, Sun F, *et al.* Tuning piezoelectric driven photocatalysis by La-doped magnetic $BiFeO_3$-based multiferroics for water purification. *Nano Energy* 2022, **93**: 106792.
[39] Tu SC, Guo YX, Zhang YH, *et al.* Piezocatalysis and piezo-photocatalysis: Catalysts classification and modification strategy, reaction mechanism, and practical application. *Adv Funct Mater* 2020, **30**: 2005158.
[40] Liu LZ, Huang HW, Chen ZS, *et al.* Synergistic polarization engineering on bulk and surface for boosting CO_2 photoreduction. *Angew Chem Int Ed* 2021, **60**: 18303–18308.
[41] Xie ZS, Tang XL, Shi JF, *et al.* Excellent piezo-photocatalytic performance of $Bi_4Ti_3O_{12}$ nanoplates synthesized by molten-salt method. *Nano Energy* 2022, **98**: 107247.
[42] Zhang DP, Li YX, Wang PF, *et al.* Regulating spin polarization through cationic vacancy defects in $Bi_4Ti_3O_{12}$ for enhanced molecular oxygen activation. *Angew Chem Int Ed* 2023, **62**: 2303807.
[43] Zheng CX, Yang H, Cui ZM, *et al.* A novel $Bi_4Ti_3O_{12}/Ag_3PO_4$ heterojunction photocatalyst with enhanced photocatalytic performance. *Nanoscale Res Lett* 2017, **12**: 608.
[44] Zhao XX, Yang H, Zhang HM, *et al.* Surface-disorder-engineering-induced enhancement in the photocatalytic activity of $Bi_4Ti_3O_{12}$ nanosheets. *Desalin Water Treat* 2019, **145**: 326–336.
[45] Yuan GQ, Zhang G, Li KZ, *et al.* Preparation and photocatalytic performance for degradation of rhodamine B of AgPt/$Bi_4Ti_3O_{12}$ composites. *Nanomaterials* 2020, **10**: 2206.
[46] Yu CY, He JJ, Tan MX, *et al.* Selective enhancement of photo-piezocatalytic performance in $BaTiO_3$ via heterovalent ion doping. *Adv Funct Mater* 2022, **32**: 2209365.
[47] Liu YB, Zhu GQ, Gao JZ, *et al.* Enhanced photocatalytic activity of $Bi_4Ti_3O_{12}$ nanosheets by Fe^{3+}-doping and the addition of Au nanoparticles: Photodegradation of Phenol and bisphenol A. *Appl Catal B Environ* 2017, **200**: 72–82.
[48] Dai CL, Feng ZH, Hu QM, *et al.* Recent progress in modification and composite strategies of graphitic carbon nitride as catalysts for heterogeneous photo-Fenton reaction. *Mater Sci Semicond Process* 2023, **167**: 107807.
[49] Cheng Y, Zhang YB, Wang ZB, *et al.* Review of Bi-based catalysts in piezocatalytic, photocatalytic and piezo-photocatalytic degradation of organic pollutants. *Nanoscale* 2023, **15**: 18571–18580.
[50] Cui YF, Guo P, Wang FH, *et al.* Self-doping based facet junctions and oxygen vacancies in ferroelectric $Bi_3Ti_xNb_{2-x}O_9$ nanosheets for boosting photocatalytic degradation and antibacterial activity. *ACS Appl Mater Interfaces* 2022, **14**: 51819–51834.
[51] Wang HP, Chen C, Jiang XP, *et al.* Cu/W co-doped $CaBi_2Nb_2O_9$ piezoelectric ceramics on structural and electrical properties. *J Alloys Compd* 2022, **896**: 163078.
[52] Du XR, Huang WH, Thatikonda SK, *et al.* Improved ferroelectric and dielectric properties of Sm, La co-doped $Bi_4Ti_3O_{12}$ multifunctional thin films with orange-red emission. *J Mater Sci Mater Electron* 2019, **30**: 13158–13166.
[53] Cao N, Chen Z, Zang KT, *et al.* Doping strain induced Bi–Ti^{3+} pairs for efficient N_2 activation and electrocatalytic fixation. *Nat Commun* 2019, **10**: 2877.
[54] Huang HW, Tu SC, Zeng C, *et al.* Macroscopic polarization enhancement promoting photo- and piezoelectric-induced charge separation and molecular oxygen activation. *Angew Chem Int Ed* 2017, **56**: 11860–11864.
[55] Tang RL, Xu W, Lian X, *et al.* Na_2CeF_6: A highly laser damage-tolerant double perovskite type Ce(IV) fluoride exhibiting strong second-harmonic generation effect. *Small* 2023, **7**: 202308348.